RESEARCH ARTICLE

Wave coupling from the lower to the middle thermosphere: Effects of mean winds and dissipation

F. Gasperini[1] , **J. M. Forbes**[2] , and **M. E. Hagan**[1]

[1]Department of Physics, Utah State University, Logan, Utah, USA, [2]Department of Aerospace Engineering Sciences, University of Colorado Boulder, Boulder, Colorado, USA

Abstract Recent observational and modeling evidence has demonstrated that planetary waves can modulate atmospheric tides, and secondary waves arising from their nonlinear interactions are an important source of both temporal and longitude variability in the thermosphere. While significant progress has been made on understanding how this form of vertical coupling occurs, uncertainty still exists on how the horizontal structures of primary and secondary waves evolve with height and the processes responsible for this evolution, in part due to lack of global observations between 120 km and 260 km. In this work we employ a Thermosphere Ionosphere Mesosphere Electrodynamics general circulation model simulation covering all of 2009 that is forced by Modern-Era Retrospective Analysis for Research and Applications dynamical fields, to assess the relative contribution of zonal mean winds and molecular dissipation on the vertical coupling of the eastward propagating diurnal tide with zonal wave number 3 (DE3), the 3 day ultrafast Kelvin wave, and the secondary waves arising from their nonlinear interaction. By developing and applying a new analytic formulation describing the latitudinal structure of an equatorially trapped wave subject to dissipation and background winds, we show that dissipation is the primary contributor to the broadening of the latitudinal structures with height, while asymmetries in the background wind field are responsible for the distortion of the height-latitude structures.

1. Introduction

There is both observational and modeling evidence that planetary waves (PWs) interact with and modulate atmospheric tides [e.g., *Beard et al.*, 1999; *Kamalabadi et al.*, 1997; *Liu et al.*, 2007, 2010; *Angelats I Coll and Forbes*, 2002; *Yamashita et al.*, 2002; *Lieberman et al.*, 2004; *Nguyen et al.*, 2016; *Pancheva et al.*, 2000, 2002; *Pancheva and Mitchell*, 2004; *Pedatella et al.*, 2012; *Pedatella and Forbes*, 2010, 2012; *Pogoreltsev et al.*, 2007; *Chang et al.*, 2009, 2011], and there are indications that PW-tide interactions may be a major source of both tidal and longitude variability in the upper atmosphere [e.g., *Pedatella and Forbes*, 2012; *Gasperini et al.*, 2015; *Yue et al.*, 2013]. A difficulty in gaining a global perspective is that the time series analyses really required to quantify PW-tide interactions can only originate in ground-based measurements, but the existing distribution of ground-based sites is inadequate to provide a global perspective. Some creative methods have been developed to provide evidence of either daily tidal variability [e.g., *Oberheide et al.*, 2002; *Lieberman et al.*, 2004] or PW-tide interactions [*Moudden and Forbes*, 2010, 2011a, 2011b; *Forbes and Moudden*, 2012] using space-based measurements, but these often introduce ambiguities in interpretation in terms of what the interacting waves are.

Before proceeding further, some notations used throughout this paper are defined. We adopt the mathematical form $A_{n,s}\cos(n\Omega t + s\lambda - \Phi_{n,s})$ to represent a tidal oscillation in any atmospheric variable, where t = time in UT, Ω = rotation rate of the Earth ($2\pi/24$ h), λ = longitude, $n = (1, 2, \ldots)$ is the subharmonic of a solar day, $s = (\ldots -2, 0, 1, 2 \ldots)$ is the zonal wave number and $A_{n,s}$ is the amplitude and $\Phi_{n,s}$ is the phase, which are functions of latitude and altitude. The positive integer $n = 1, 2, \ldots$ corresponds to oscillation periods of 24 h, 12 h, $\ldots$ and are referred to as diurnal and semidiurnal tides, respectively. In this context, s > 0 (s < 0) components correspond to westward (eastward) propagating tides. The phase is defined as the time of maximum at 0° longitude, which is the local time of maximum at Greenwich. The notation DWx (DEx) denotes a westward (eastward) propagating diurnal tide with zonal wave number $x = s$, for semidiurnal and terdiurnal tides S and T replaces D. Standing tidal oscillations (i.e., $s = 0$) are denoted as D0 and S0, and waves with $n = 0$ are referred to as stationary planetary waves (SPW).

Modulation of a tide by a PW is thought to occur through a nonlinear quadratic interaction that results in the generation of "sum" and "difference" secondary waves (SWs) [*Teitelbaum and Vial*, 1991]. The interaction between a PW with frequency $\Delta\omega$ and zonal wave number m, i.e., $\cos(\Delta\omega t + m\lambda - \Phi_{n,s})$, with a tide with frequency $n\Omega$ and zonal wave number s, $\cos(n\Omega t + s\lambda)$, thus yields sum and difference secondary waves (hereafter SW$^+$ and SW$^-$), with frequencies $n\Omega \pm \Delta\omega$ and zonal wave numbers $s \pm m$. In the spectrum of a time series, long-period PW ($\Delta\omega << n\Omega$) appears as two sideband peaks on either side of the main tidal peak at frequency $n\Omega$. A well-documented example is modulation of the migrating (Sun-synchronous, westward propagating) semidiurnal tide ($n = 2$, $s = 2$) with the westward propagating quasi-2 day wave QTDW ($n = 0.5$, $s = 3$) [*Cevolani and Kingsley*, 1992; *Beard et al.*, 1999; *Manson et al.*, 1982; *Harris and Vincent*, 1993; *Thayaparan et al.*, 1997a, 1997b; *Palo et al.*, 1999]. The SWs are a westward propagating 9.6 h wave with $s = 5$ and an eastward propagating 16 h wave with $s = -1$; the zonal wave numbers obviously cannot be differentiated using ground-based observations.

Other examples in model simulations [*Pedatella et al.*, 2012] are the modulations of DE3 and DW1 by the quasi-6 day wave (Q6DW), which produce secondary waves with respective periods and zonal wave numbers of of (20 h, $s = -2$; 28 h, $s = -4$) and (20 h, $s = 2$; 28 h, $s = 0$). Satellite-based experimental evidence for these and other Q6DW-tide interactions is provided by *Forbes and Zhang* [2017]. Another type of interaction that produces SW is tide-tide nonlinear interactions; *Hagan et al.* [2009] demonstrate that DE3 and DW1 can interact to produce SE2 and SPW4, and *Moudden and Forbes* [2013] show that various interactions between diurnal and semidiurnal tides produce a variety of terdiurnal tides over a range of wave numbers ($s = -1$ to $s = +5$). Nonlinear interactions have also been shown to occur between lunar tide and PW variability in the dynamics driving Sq currents, and solar-driven variability in the E region conductivity [*Gasperini and Forbes*, 2014; *Elhawary and Forbes*, 2016].

Another important point raised in numerical simulations [*Palo et al.*, 1999; *Pedatella et al.*, 2012] and observations [*Moudden and Forbes*, 2013] is that SWs tend to propagate away from their sources as independent oscillations. Moreover, each SW is expected to be affected differently by the background wind field depending on its zonal wave number and Doppler-shifted frequency; at some distance from the source, one of the SW could be significantly larger than the other, either due to propagation conditions or because the two waves are not excited with equal efficiency. It is also possible that SW can be observed either in the presence or absence of either or both of the primary waves. A good example of this is in the simulations of *Palo et al.* [1999], where the SWs due to QTDW-SW2 interaction propagate well above 100 km, whereas the QTDW does not. *Nguyen et al.* [2016] showed that the secondary wave response due to QTDW-DW1 interactions is the most sensitive to the nonlinear forcing occurring in the lower and middle mesosphere, and not coincident with the regions of strongest nonlinear forcing. Additionally, the two secondary waves do not seem to be excited with equal efficiency in these interactions, and the underlying physical cause is a topic of current research.

The observational studies cited above are confined to altitudes below about 100 km. However, *Gasperini et al.* [2015] use temperature measurements from the Sounding of the Atmosphere using Broadband Emission Radiometry (SABER) instrument on board the Thermosphere Ionosphere Mesosphere Energetics Dynamics at 110 km and Gravity Field and Steady-State Ocean Circulation Explorer (GOCE) density and wind measurements near 260 km to demonstrate that DE3 and a 3 day ultrafast Kelvin wave (UFKW) serve to dynamically couple these altitudes. DE3 and the UFKW are two prominent Kelvin waves of tropospheric origin that preferentially propagate into the ionosphere-thermosphere (IT) system, and modify satellite drag [e.g., *Forbes et al.*, 2009; *Oberheide et al.*, 2009], ionospheric densities [*Chang et al.*, 2011; *Gu et al.*, 2014; *Pedatella and Forbes*, 2009], and even GPS scintillations (S4 index) to a significant degree [*Liu et al.*, 2013]. Moreover, *Gasperini et al.* [2015] show that nonlinear interactions between DE3 and the UFKW generate SW that participate in this coupling. The SW amplitudes are often half or more than that of the primary waves and add spatial-temporal complexity to the neutral dynamics since their periods and zonal wave numbers are different than those of the primary waves. Considering that these waves extend well beyond tropical latitudes (i.e., $\pm 45°$ geomagnetic latitude) and are displaced from the geomagnetic coordinate frame, this complexity is likely to carry over to the ionosphere through neutral-plasma collisions, i.e., in terms of tidal-induced sporadic E layers and dynamo-generated electric fields that redistribute F region ionization, widely expanding the scope of relevance of the problem.

Gasperini et al. [2015] note that the coupling between 110 km and 260 km is imperfect; that is, differences in the spatial-temporal structures of DE3, the UFKW and SW existed between these two altitudes. This led them

to surmise that this was due to the effects of mean winds and dissipation in the intervening altitudes. This conjecture motivates the present paper, which employs a general circulation model (GCM) to answer the following questions: What are the relative roles of mean winds and dissipation in determining the height versus latitude structures of DE3 and UFKW in the thermosphere, and the SWs that result from their nonlinear interaction? And what is the nature of the SW in terms of classical atmospheric wave theory? The following section discusses the general circulation model (GCM) employed for this study and demonstrates that it contains DE3, UFKW, and SW with similar amplitudes and variability as the observations analyzed by *Gasperini et al.* [2015]. This sets the stage for a thorough analysis of the latitude versus height structures of these waves in section 3, and in particular how mean winds and dissipation serve to affect these structures. Our conclusions are provided in section 4.

## 2. Models and Methods

2.1. MERRA-Forced TIME-GCM

In this work we employ a Thermosphere Ionosphere Mesosphere Electrodynamics general circulation model (TIME-GCM) simulation covering all of 2009 that is forced by interpolated 3-hourly Modern-Era Retrospective Analysis for Research and Applications (MERRA) dynamical fields at the lower boundary of ~30 km, as described by *Häusler et al.* [2014].

TIME-GCM is one of several time-dependent National Center for Atmospheric Research models developed to simulate the circulation, temperature, electrodynamics, and compositional structure of the upper atmosphere and ionosphere. TIME-GCM is a global grid point model that calculates neutral gas heating, dynamics, photoionization, electrodynamics, and composition of the middle and upper atmosphere and ionosphere from first principles for a given solar irradiance spectrum which varies with solar activity. It predicts global neutral winds, constituents, electron and ion densities, temperatures and drifts, and the dynamo electric field. TIME-GCM inherently accounts for atmospheric tides that are excited by the absorption of ultraviolet and extreme ultraviolet radiation in the middle and upper atmosphere. Upward propagating waves excited in the troposphere are specified at the ~30 km lower boundary. TIME-GCM provides a global simulation of the vertical evolution of the wave spectrum through the middle atmosphere, thermosphere, and ionosphere, and its effects on the ionosphere. We refer the reader to *Roble et al.* [1988], *Richmond et al.* [1992], *Roble and Ridley* [1994], and references therein for a more complete description of the TIME-GCM.

MERRA is a NASA satellite-era reanalysis that uses a major new version of the Goddard Earth Observing System Data Assimilation System Version 5 (GEOS-5) [*Rienecker et al.*, 2011]. MERRA is a physics-based model with a horizontal resolution of 1.25°, temporal resolution of 3 h, and 42 vertical levels ranging from 1000 hPa to 0.1 hPa (~64 km). For this work, we choose MERRA due to its comprehensive nature, especially in terms of the hydrological cycle (relevant to lower wave forcing), and because it provides 3-hourly data enabling both diurnal and semidiurnal tides to be extracted on a daily basis. A number of studies have used MERRA to study regional and global climate, various types of wave coupling, precipitation, stratospheric water vapor, global energy, and water budgets. Additionally, *Lindsay et al.* [2014] analyzed seven different reanalysis products (including various versions of National Centers for Environmental Prediction and European Centre for Medium-Range Weather Forecasts), finding MERRA to outperform the other models. The MERRA lower boundary condition provides a highly improved method to specify the upward propagating wave spectrum (with periods of 12 h or greater) at 30 km altitude, compared for instance to the Global Scale Wave Model [*Häusler et al.*, 2014].

The simulation herein implemented uses the high-resolution version of the TIME-GCM, corresponding to $2.5° \times 2.5°$ in latitude and longitude, four grid points per scale height in the vertical direction, and 60 s time step. The 3-hourly MERRA resolution inherently accounts for the variability in the diurnal and semidiurnal tides, as well as the PWs, generated in the troposphere. The MERRA lower boundary condition provides an excellent state-of-the-art specification of the upward propagating wave spectrum at 30 km altitude, whereas the TIME-GCM provides a state-of-the-art global simulation of the vertical evolution of this wave spectrum through the thermosphere.

Figure 1 shows the latitude versus zonal wave number and the latitude versus period representation of the main diurnal tides and short-period (2-6 days) eastward propagating waves with $s = -1$ present in the 2009 MERRA/TIME-GCM temperatures at 260 km (a and b) and 110 km (a' and b'). The main nonmigrating diurnal tides are DE3, DE2, DE1, and DW2; while the dominant short-period wave is a UFKW with period ranging from
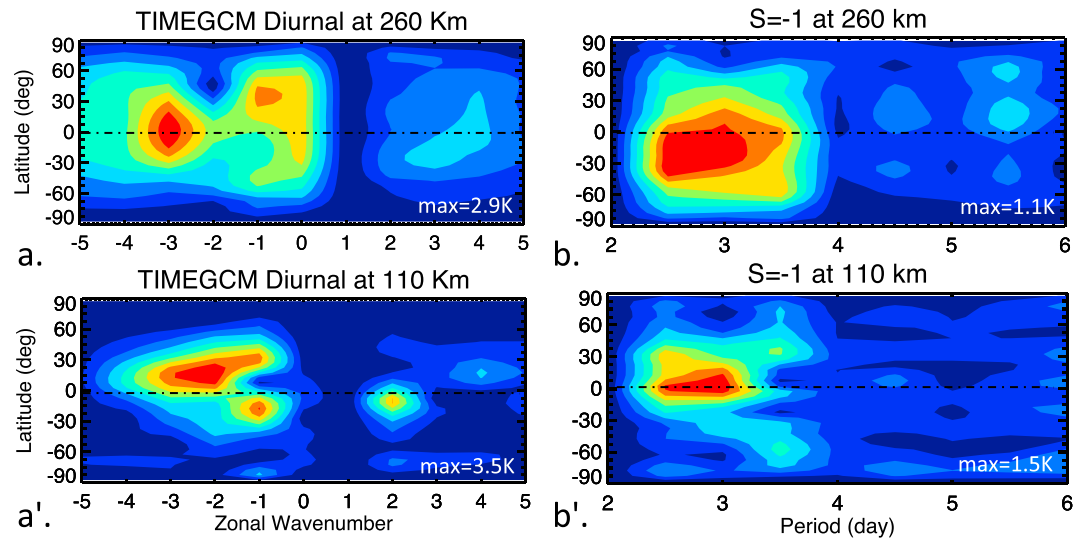
Figure 1. Latitude versus zonal wave number plot of the diurnal tide at (a) 260 km and (a′) 110 km, and latitude versus period plot for zonal wave number −1 at (b) 260 km and (b′) 110 km for 2009 MERRA-forced TIME-GCM. Strong DE3 amplitudes are observed at both heights, with significant latitudinal asymmetry in DE3 at 110 km. The presence of a strong 2.5–3.5 day UFKW signal is also clear.
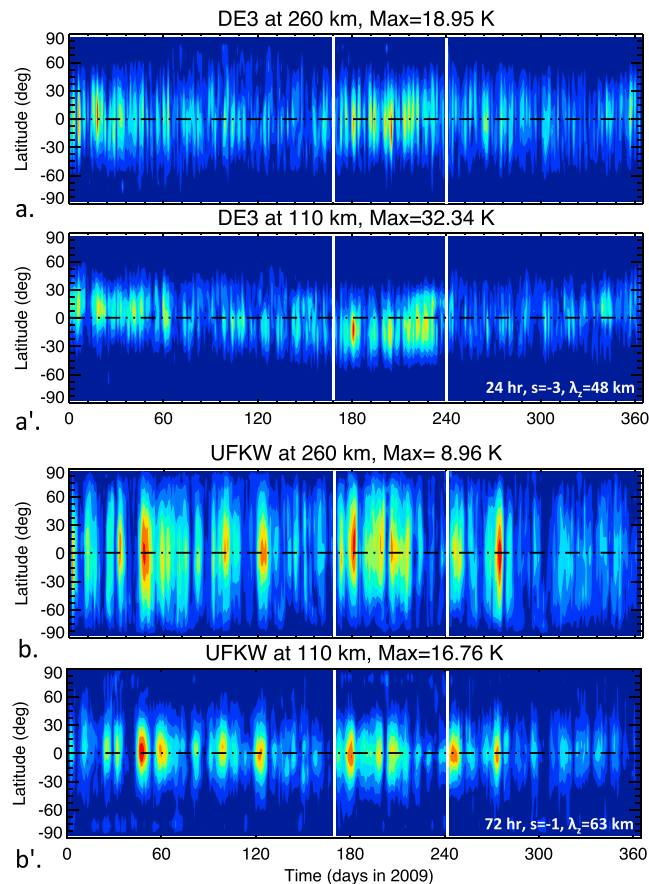
Figure 2. Time series of daily DE3 temperate amplitudes at (a) 260 km and (a′) 110 km, and 3 day UFKW amplitudes at (b) 260 km and (b′) 110 km during 2009. Large day-to-day and seasonal variability at both heights is present. Amplitudes up to 32 K (17 K) are found in DE3 (UFKW) at 110 km and up to 19 K (9 K) in DE3 (UFKW) at 260 km. Similar intraseasonal and interseasonal variability between the two heights, with some degree of asymmetry, is especially evident in DE3 at 110 km. Latitudinal broadening with height is also clear. Note that the white vertical lines indicate the 70 day period analyzed in Figure 3.
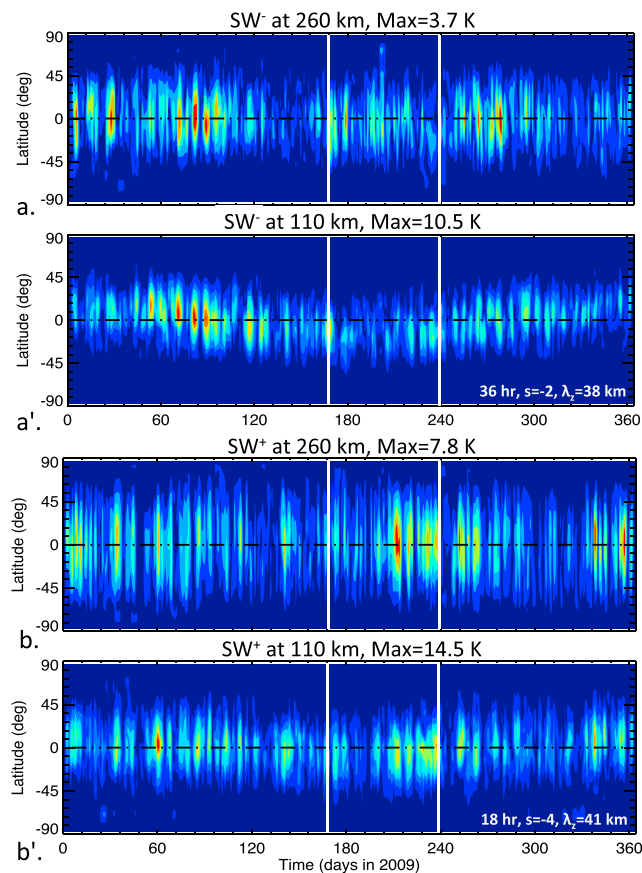
Figure 3. Similar to Figure 2 but for (a and a′) SW⁻ (36 h/$s = -2$) and (b and b′) SW⁺ (18 h/$s = -4$). Large day-to-day and seasonal variations at both heights are evident, similar to DE3 and UFKW. Amplitudes up to 11 K (15 K) are found in SW⁻ (SW⁺) at 110 km and up to 4 K (8 K) in SW⁻ (SW⁺) at 260 km. SW⁻ at 110 km is more antisymmetric than SW⁺ at the same height due to its longer first antisymmetric mode (as shown in Figure 4). SW⁺ exhibits larger amplitudes for most of the year, likely because of its higher frequency and longer vertical wavelength (and thus is less affected by dissipation).

2.5 to 3.5 days. In order to confine the present work to reasonable size and focus on the objective stated in section 1, i.e., revealing the effect of mean winds and dissipation on the latitude-height structures, only DE3, UFKW, SW⁻, and SW⁺ are further analyzed. Note that Figure 1 displays only short-period waves with $s = -1$, since those with $s \neq -1$ are found to possess amplitudes smaller than the UFKW and are not of interest for this study.

2.2. DE3, UFKW, and Their Sidebands

As explained in section 1, the modulation of a tide by a PW occurs through a nonlinear quadratic interaction producing "sum" (SW⁺) and "difference" (SW⁻) secondary waves. In the case of DE3 ($n = 1$ and $s = -3$) interacting with a 3 day UFKW ($\Delta\omega = \frac{\Omega}{3}$ and $m = -1$), SW⁺ has a frequency $n\Omega + \Delta\omega = 1.33$ day⁻¹ (i.e., 18 h period) and zonal wave number $s + m = -4$, while SW⁻ has a frequency $n\Omega - \Delta\omega = 0.66$ day⁻¹ (i.e., 36 h period) and zonal wave number $s - m = -2$. Figure 2 shows the latitude-temporal variability of DE3 and UFKW temperature amplitudes at 260 km (a and b) and 110 km (a′ and b′), while Figure 3 presents the latitude-time structures for SW⁻ and SW⁺ also at 260 km (a and b) and 110 km (a′ and b′). For each pressure level and 5° latitude bin, DE3, UFKW, SW⁺, and SW⁺ amplitudes are extracted by least squares fitting model temperatures with a time-longitude resolution of 1 h × 5°. In order to reduce the uncertainties in the derived amplitudes, for each wave we perform the fit on a moving window with width equal to twice its period (i.e., 48 h for DE3, 144 h for the UFKW, 36 h for SW⁺, and 72 h for SW⁻).

All the waves display significant day-to-day variability, with low-latitude maxima of ∼32 K (∼19 K) in DE3, ∼17 K (∼9 K) in UFKW, ∼11 K (∼4 K) in SW⁻, and ∼15 K (∼8 K) in SW⁺ at 110 km (260 km). Both primary and secondary waves possess similar amplitudes and intermittency to those found in SABER and GOCE
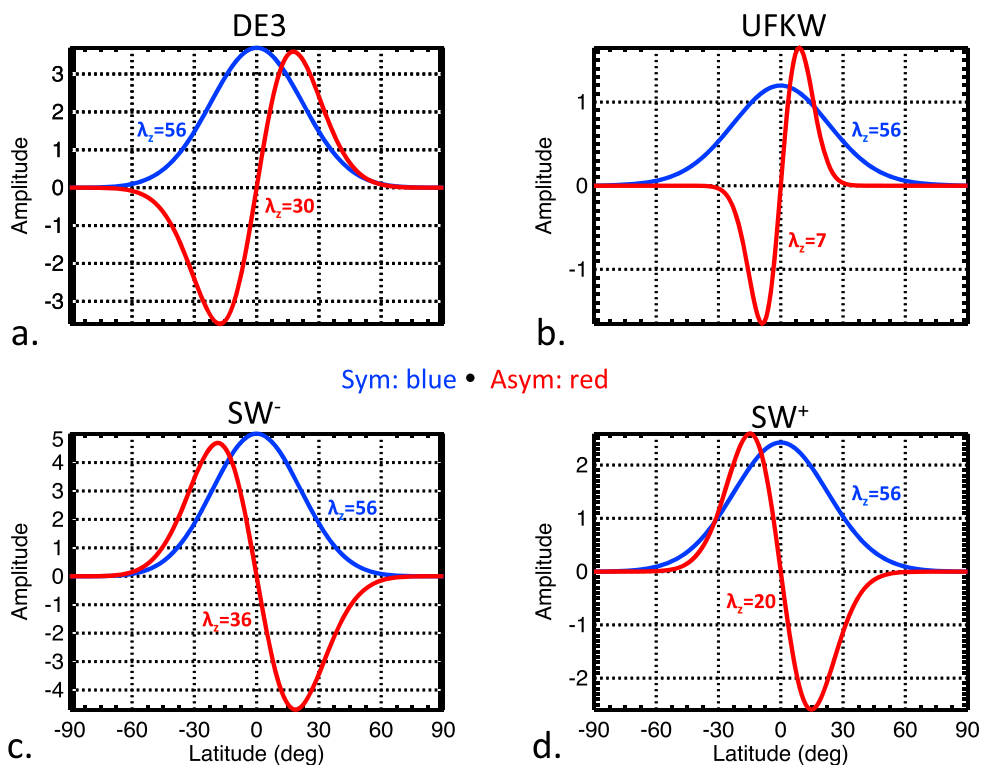
Figure 4. First symmetric (blue) and first antisymmetric (red) Hough modes of (a) DE3, (b) UFKW, (c) SW⁻, and (d) SW⁺. The vertical wavelength is also indicated in each panel (in kilometers), i.e., 56 km for all the first symmetric modes and 30 km, 7 km, 36 km, and 20 km for the first antisymmetric mode of DE3, UFKW, SW⁻, and SW⁺, respectively.

measurements [*Gasperini et al.*, 2015], although the latter corresponds to 2011 and not 2009. Similar to what is reported by *Gasperini et al.* [2015], there is no exact one-to-one correspondence between the latitude-time structures of the waves at 110 km and those at 260 km. As one can appreciate by observing the longer period trend in latitude-time evolution of the waves (Figures 2 and 3), DE3 and SW⁻ possess a significant antisymmetric component at 110 km that is not present at 260 km (or in UFKW, SW⁺). Furthermore, one can see that for most of the year, and especially at 260 km, SW⁺ exhibits larger amplitudes than SW⁻. Both the greater antisymmetric component at 110 km and larger amplitudes for the shorter-period secondary wave (i.e., 18 h for SW⁺) are similar to what is reflected in the observations shown by *Gasperini et al.* [2015].

2.3. Interpretation in Terms of Classical Tidal Theory

To facilitate the interpretation of the horizontal structures exhibited by the waves in Figures 2 and 3, we use the results of classical tidal theory. In the classical theory of atmospheric tides [*Chapman and Lindzen*, 1970], where the background atmosphere is assumed to be inviscid and independent of latitude, the linearized response to thermal or gravitational forcing reduces to an eigenfunction-eigenvalue problem where the eigensolutions (Hough functions) of Laplace's tidal equation describe the horizontal structures of each mode, and the eigenvalues (equivalent depths) fix each mode's vertical structure. Each Hough mode is a function of latitude and may be expressed as an infinite sum of associated Legendre polynomials. Practically speaking, it is substantially efficient to fit the tidal component by means of orthogonal Hough functions, as only a few Hough functions are necessary to provide good fitting results.

Figure 4 shows the Hough functions for the first symmetric (blue line) and first antisymmetric (red line) mode of DE3 (a), UFKW (b), SW⁻ (c), and SW⁺(d), with their associated vertical wavelengths (in kilometers) derived assuming an isothermal ($T = 256$ K), motionless, and inviscid atmosphere. The first symmetric mode of all the waves examined follows a Gaussian distribution centered at the equator with a vertical wavelength ~56 km, while the first antisymmetric mode has two separate nodes with a maximum/minimum around $\pm10-20°$ latitude and a vertical wavelength of ~30 km for DE3, ~7 km for UFKW, ~36 km for SW⁻, and ~20 km for SW⁺. Note that these are the vertical wavelengths calculated from the wave's frequency and zonal wave number alone and assuming isothermal, motionless, and inviscid conditions. Using the vertical progression
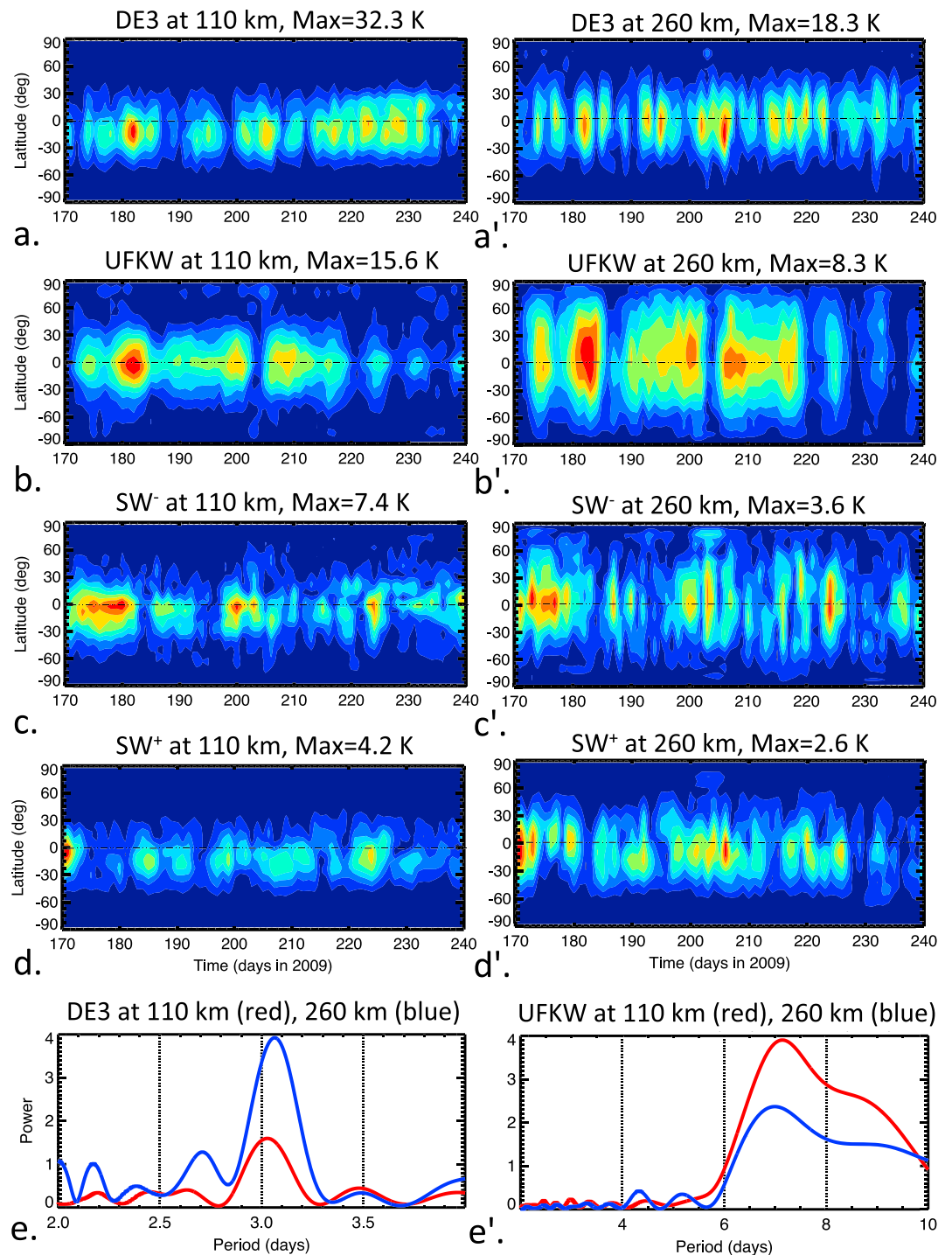
Figure 5. Latitude-time representation for the 70 day period from DOY 170 to DOY 240 of (a) DE3 (*a'*), (b) UFKW (*b'*), (c) SW⁻ (*c'*), (d) SW⁺ (*d'*) amplitudes at 110 km (260 km). (*e* and *e'*) The periodogram of DE3 and UFKW at 110 km (red line) and 260 km (blue line). Note the strong 3 day modulation of DE3 amplitudes due to the interaction with the UFKW and a quasi-7 day oscillation in the UFKW (this variation could not be traced back to any specific nonlinear interaction).

of the phases between 70 km and 120 km, we also calculated the vertical wavelengths consistent with the model temperatures. These are found to vary slightly day by day and to be in the range 52–55 km for DE3, 59–61 km for UFKW, 41–44 km for SW⁻, and 39-42 km for SW⁺. These values are in line with a mixture of symmetric and antisymmetric modes for all the waves examined and are similar to what is reported by *Truskowski et al.* [2014] for DE3 and *Forbes* [2000] for a 3 day Kelvin wave.

It is well known that the efficiency with which a given wave propagates into the thermosphere system depends on its period and vertical wavelength, the shorter-period and longer-wavelength waves being less affected by dissipation and thus being more capable of propagating to high altitudes [*Forbes and Garrett*, 1979]. The longer vertical wavelength for DE3's ($\lambda_z = 30$ km) and SW⁻'s ($\lambda_z = 36$ km) first antisymmetric mode explains the larger antisymmetric component observed in DE3 and SW⁻ at 110 km, as shown in Figures 2a′ and 3a′, respectively. Additionally, SW⁺'s shorter period (i.e., higher frequency) means that SW⁺ is less affected by dissipation in the lower thermosphere than SW⁻, given that they possess approximately the same vertical wavelength. As a result, the amplitudes of SW⁺ are generally larger than those of SW⁻. This is especially evident at 260 km, at which altitude the antisymmetric modes have been mostly dissipated due to their shorter vertical wavelengths.

In order to better assess some of the day-to-day variability and more clearly show the differences between the latitude-temporal structures at 110 km and those at 260 km, Figure 5 shows the time series of DE3 (a and a′), 3 day UFKW (b and b′), SW⁻ (c and c′), and SW⁺ (d and d′) for the 70 day period ranging from day of year (DOY) 170 to DOY 240 (indicated by white vertical lines in Figures 2 and 3) at 110 km and 260 km. This period is chosen because both primary and secondary waves exhibit large amplitudes. Amplitudes up to 32 K (18 K) are found in DE3 and 16 K (8 K) in UFKW at 110 km (260 km); while SW⁻ and SW⁺ possess amplitudes up to 8 K (4 K) and 10 K (4 K) at 110 km (260 km), respectively.

Interestingly, and similar to the observational results presented by *Gasperini et al.* [2015], there is no clear correlation between the maxima in the sidebands and the maxima in DE3 and UFKW. This could be explained by nonlinear interactions occurring at lower heights. As reported by *Nguyen et al.* [2016], secondary waves propagate vertically away from the generation region (e.g., mesosphere) as independent waves and are affected by dissipation and mean winds differently than the primary waves. The modulation of DE3 by the 3 day UFKW is also evident in the time series of DE3 (see Figures 5a and 5a′), where a clear 3 day modulation can be seen both at 110 km and 260 km. Figure 5e, showing the equatorial periodogram of daily DE3 amplitudes at 110 km (red line) and 260 km (blue line), contains evidence of this 3 day modulation. Looking at Figures 5b and 5b′, one can also see a ∼7 day modulation of the UFKW amplitudes, confirmed by the periodogram displayed in Figure 5e′. Investigating the origin of this modulation, possibly associated to the interaction of the UFKW with a longer period PW or a modulation in the low-atmosphere forcing, is beyond the scope of this work and is left for future investigations.

2.4. Analytic Formulation

In this subsection an approximate analytic solution to the momentum equations is derived that describes some salient features of upward propagating waves in the thermosphere subject to the joint effect of dissipation and mean winds. The results of this subsection are then used to elucidate the height-latitude structures shown by the waves (i.e., Figures 6–9).

The joint presence of diffusion (i.e., momentum and heat) and planetary rotation renders the governing equations inseparable in height and latitude (meaning that the height structures vary with latitude, or equivalently, the horizontal structures vary with height) in the thermosphere, thus requiring a numerical solution to the problem. Here we make some simplifying assumptions to isolate the essential influences of dissipation as it applies to the current problem. Following the methodology of *Holton and Lindzen* [1968], we use the so-called beta-plane (or β-plane) [*Lindzen*, 1967a] approximation to find a solution to the momentum equations for equatorially trapped waves with negligible meridional velocity (Kelvin waves, e.g., DE3 and UFKW). Moreover, we extend their derivation to arrive at an expression describing the latitudinal structure of these waves in a rotating atmosphere subject to dissipation and zonal mean winds. (Note that, in this work, zonal mean and longitude mean are synonymous and also imply local time mean.)

On a rotating sphere, such as Earth, the Coriolis parameter $f = 2\Omega\sin\theta$ varies with the sine of latitude. In the β-plane approximation the curved surface of Earth is replaced locally by a plane, but the Coriolis parameter f is allowed to vary linearly in the north-south direction. Explicitly, the Coriolis parameter is given approximately

June Solstice
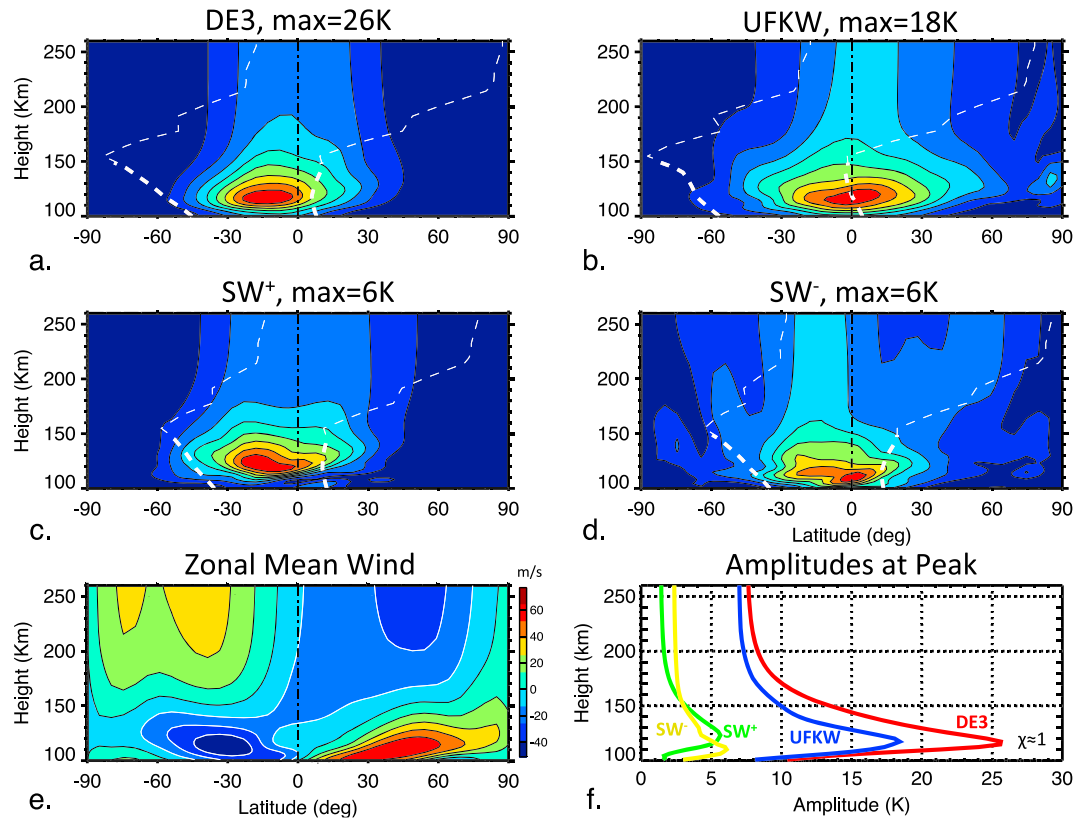
Figure 6. Height versus latitude structures for June solstice (i.e., DOY 172) of (a) DE3, (b) UFKW, (c) SW$^+$, (d) SW$^-$ temperature amplitudes in comparison to the (e) zonal mean wind field. Note that the amplitude maxima tend to occur in the region where the zonal mean winds are maximum westward (negative values, i.e., blue colors), and the waves tend to follow the westward wind regime up to 260 km. The white dashed line represents the e^{-1} width calculated from equation (16) and is centered on the latitude of westward wind maxima. (f) The vertical profile of DE3, UFKW, SW$^+$, and SW$^-$ maximum amplitudes between 100 km and 260 km ($\chi = 1$ denotes the region where the wave maximizes, i.e., $\sigma_D \approx \nu_r$).

by $f \approx f_0 + \beta y$, in which y is the meridional distance from some fixed latitude, f_0 is a mean Coriolis parameter, and β (from which the beta plane gets its name) is the meridional gradient of f at that fixed latitude. The advantage of the β-plane approximation over more accurate formulations is that it captures the most important dynamical effects of sphericity for the study of equatorial and midlatitude flow, without the complicating geometric effects, which are not essential to describe the salient features of many phenomena.

The linearized eastward (u) and northward (v) momentum equations for a rotating atmosphere on a background state, which include eddy and molecular dissipation, ion drag, and zonal mean winds $\bar{U}$, can be written as [*Forbes and Garrett*, 1979]:

$$\frac{\partial u}{\partial t} + \frac{\bar{U}}{a\cos\theta}\frac{\partial u}{\partial \phi} - 2\Omega\sin\theta v = -\frac{1}{a\rho_0\cos\theta}\frac{\partial p}{\partial \phi} + \left(\kappa_{\text{eddy}} + \frac{\mu}{\rho_0}\right)\frac{\partial^2 u}{\partial z^2} - \lambda_{\text{ion}}u, \tag{1}$$

$$\frac{\partial v}{\partial t} + \frac{\bar{U}}{a\cos\theta}\frac{\partial v}{\partial \phi} + 2\Omega\sin\theta u = -\frac{1}{a\rho_0}\frac{\partial p}{\partial \theta} + \left(\kappa_{\text{eddy}} + \frac{\mu}{\rho_0}\right)\frac{\partial^2 v}{\partial z^2} - \lambda_{\text{ion}}\sin^2 I v. \tag{2}$$

where ϕ and θ are the longitude and latitude, Ω is the Earth's rotation rate, a is the Earth's radius, p is the pressure, λ_{ion} is the ion drag coefficient, I is the magnetic dip angle, and ρ_0 is the neutral density. Because of the predominant dependence of ρ_0 on height, we ignore its horizontal variation. Note that this is a very common approximation [see, e.g., *Forbes and Garrett*, 1979]. Mean meridional winds were also omitted due to their small amplitude.
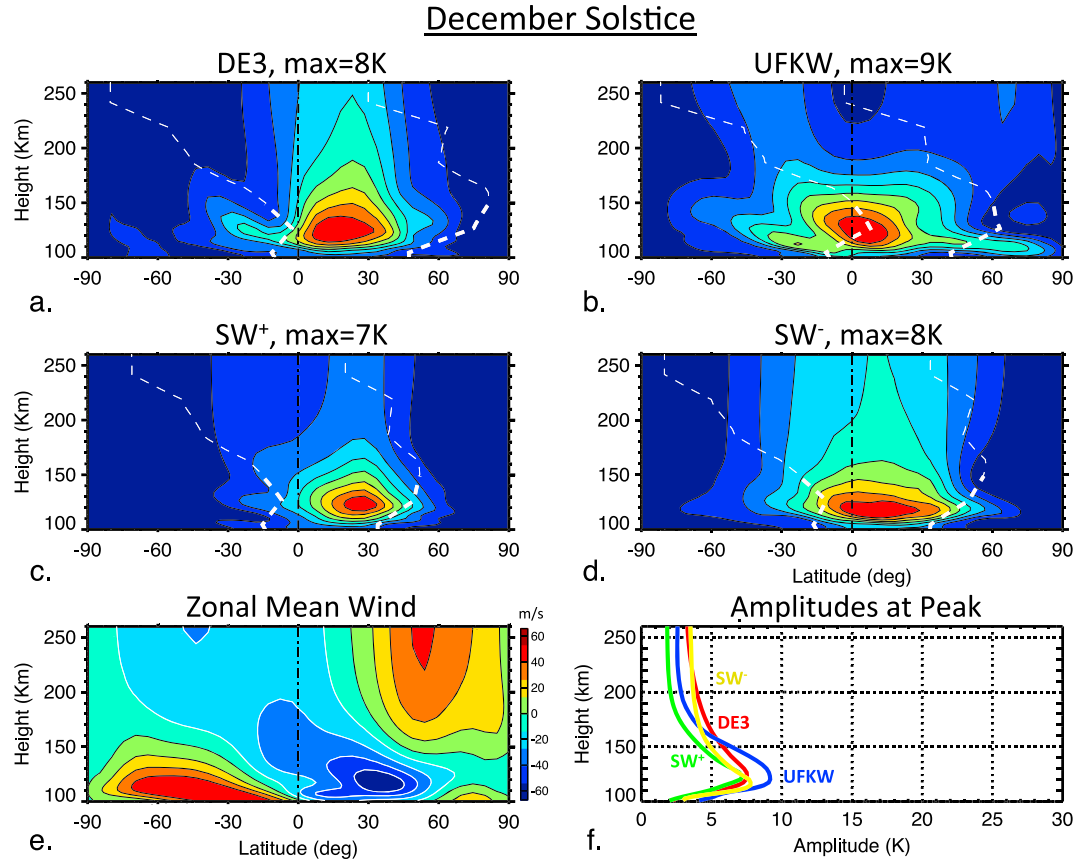
December Solstice

Figure 7. Same as Figure 6 but for December solstice (i.e., DOY 355). Note that, opposite than the March solstice, the low-thermosphere (110–150 km) winds are mainly eastward (positive values, i.e., red colors) in the Southern Hemisphere and westward (negative values, i.e., blue colors) in the Northern Hemisphere. All the waves tend to follow the westward wind regime up to 260 km, similar to what is shown in Figure 6 for the June solstice.

Using the equatorial β-plane approximation ($f_0 = 0$), around the equator $\sin\theta \simeq \theta = y/a$ and $\cos\theta \simeq 1$, so $2\Omega\sin\theta = \frac{2\Omega y}{a} = \beta y$, where $\beta = \frac{2\Omega}{a}$, equations (1) and (2) can be written as

$$\frac{\partial u}{\partial t} + \bar{U}\frac{\partial u}{\partial x} - \beta y v = -\frac{1}{\rho_0}\frac{\partial p}{\partial x} + \left(\kappa_{\text{eddy}} + \frac{\mu}{\rho_0}\right)\frac{\partial^2 u}{\partial z^2} - \lambda_{\text{ion}}u, \tag{3}$$

$$\frac{\partial v}{\partial t} + \bar{U}\frac{\partial v}{\partial x} + \beta y u = -\frac{1}{\rho_0}\frac{\partial p}{\partial y} + \left(\kappa_{\text{eddy}} + \frac{\mu}{\rho_0}\right)\frac{\partial^2 v}{\partial z^2} - \lambda_{\text{ion}}\sin^2 l v. \tag{4}$$

If we assume a periodic solution of the form $u, v, p \propto \hat{u}, \hat{v}, \hat{p}\, e^{i(\sigma_D t + \frac{s}{a}x + k_z z)}$, then the terms $\frac{\partial}{\partial t} + \bar{U}\frac{\partial}{\partial x}$ are equal to $i\left(\sigma + \frac{s\bar{U}}{a}\right) = -i\sigma_D$, where $\sigma_D = \sigma + \frac{s\bar{U}}{a}$ is the Doppler-shifted (or intrinsic) frequency. With these assumptions, equations (3) and (4) become

$$i\sigma_D\hat{u} - \beta y\hat{v} = -\frac{1}{a\rho_0}is\hat{p} - \left[\left(\kappa_{\text{eddy}} + \frac{\mu}{\rho_0}\right)k_z^2 + \lambda_{\text{ion}}\right]\hat{u}, \tag{5}$$

$$i\sigma_D\hat{v} + \beta y\hat{u} = -\frac{1}{\rho_0}\frac{\partial\hat{p}}{\partial y} - \left[\left(\kappa_{\text{eddy}} + \frac{\mu}{\rho_0}\right)k_z^2 + \lambda_{\text{ion}}\sin^2 l\right]\hat{v}. \tag{6}$$

We now want to verify whether there is a solution for which v is identical to 0 ($v \equiv 0$). For this case, equation (5) becomes

$$i\sigma_D\hat{u} = -\frac{1}{a\rho_0}is\hat{p} - \left[\left(\kappa_{\text{eddy}} + \frac{\mu}{\rho_0}\right)k_z^2 + \lambda_{\text{ion}}\right]\hat{u}. \tag{7}$$
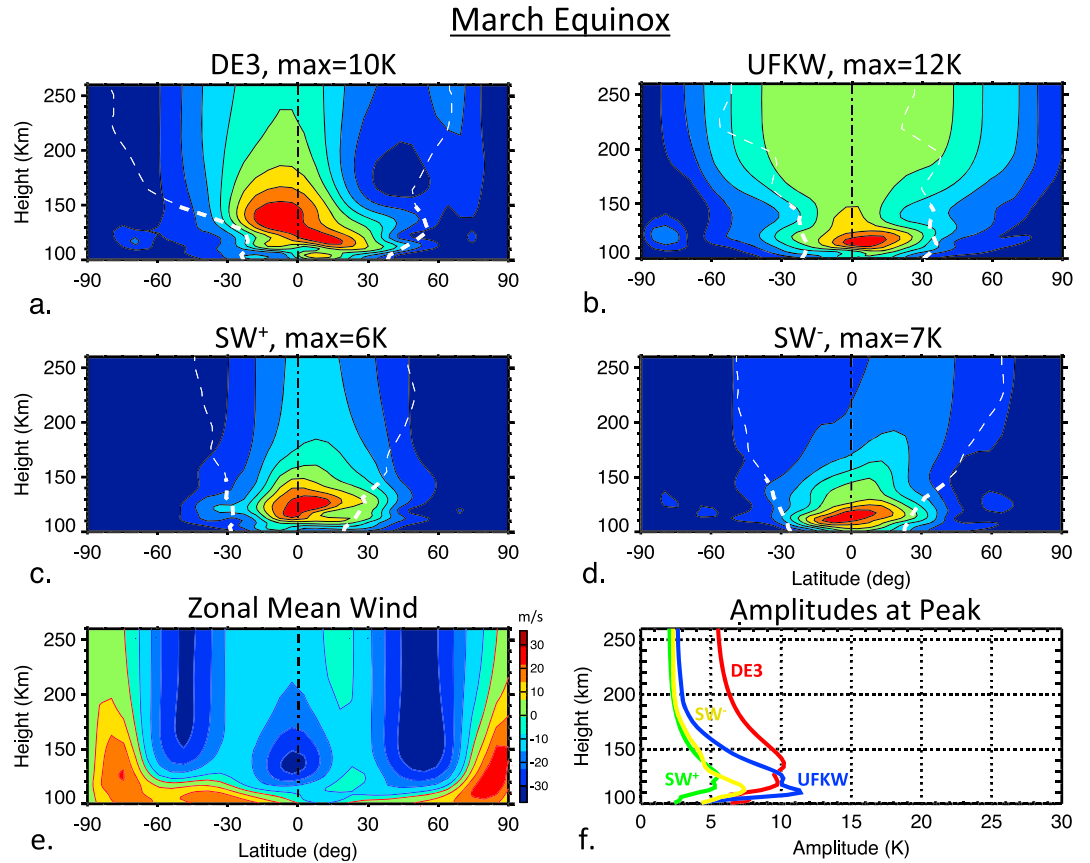
March Equinox

Figure 8. Same as Figure 5 but for March equinox (DOY 81). Note the symmetry in the background winds, with a low-latitude westward maximum at the equator and other two westward maxima around latitude ±50°. Similar to what shown in Figures 6 and 7, all the waves tend to follow the westward wind regime up to 260 km.

With some algebraic manipulations, equation (7) can be written as $i\left[\sigma_D\hat{u} - i\left[\left(\kappa_{\text{eddy}} + \frac{\mu}{\rho_0}\right)k_z^2 + \lambda_{\text{ion}}\right]\right]\hat{u} = -\frac{1}{a\rho_0}is\hat{p}$. Calling the dissipative term $\left(\frac{2\pi}{\lambda_z}\right)^2\left(\kappa_{\text{eddy}} + \frac{\mu}{\rho_0}\right) + \lambda_{\text{ion}} = \nu_r$, where ν_r is the Rayleigh friction coefficient and k_z is expressed as $k_z = 2\pi/\lambda_z$ [*Vial and Teitelbaum*, 1984; *Forbes and Hagan*, 1988], the zonal and meridional momentum equations can be rewritten as

$$i(\sigma_D - i\nu_r)\hat{u} = -\frac{1}{a\rho_0}is\hat{p}, \tag{8}$$

$$\beta y\hat{u} = -\frac{1}{\rho_0}\frac{\partial\hat{p}}{\partial y}. \tag{9}$$

As a first-order approximation and in order to find a closed analytic solution to the equations, we assume $\bar{U}$ to be latitude independent within ±20° of its latitudinal maximum ($\frac{\partial\bar{U}}{\partial y} \approx 0$, i.e., $\frac{\partial\sigma_D}{\partial y} \approx 0$). Thus, taking the y derivative of equation (8) yields the expression $i(\sigma_D - i\nu_r)\frac{\partial\hat{u}}{\partial y} = -\frac{1}{a\rho_0}is\frac{\partial\hat{p}}{\partial y}$, which can be written as

$$-\frac{1}{\rho_0}\frac{\partial\hat{p}}{\partial y} = \frac{a}{s}(\sigma_D - i\nu_r)\frac{\partial\hat{u}}{\partial y}. \tag{10}$$

Substituting equation (10) into equation (9), we derive the expression

$$\beta y\hat{u} = \frac{a}{s}(\sigma_D - i\nu_r)\frac{\partial\hat{u}}{\partial y}, \tag{11}$$

which can be written as

$$\frac{\partial\hat{u}}{\partial y} - \frac{s\beta}{a(\sigma_D - i\nu_r)}y\hat{u} = 0. \tag{12}$$
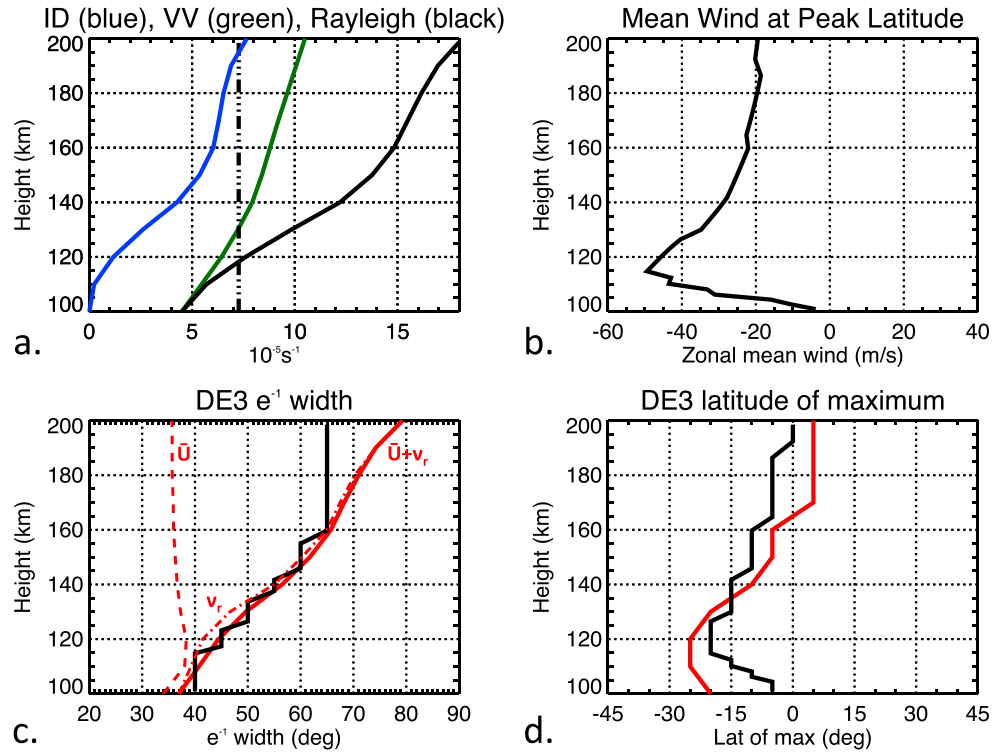
Figure 9. (a) Ion drag (blue line, from *Richmond* [1970]), vertical viscosity (green line, from *Hickey et al.* [2011] for DE3 (λ_z = 59 km), and their sum (black line, i.e., Rayleigh friction coefficient). The black dashed vertical line in Figure 9a shows the location where the frequency is equal to Earth's rotation rate Ω. (b) Zonal mean winds averages $\pm 20°$ from the latitudinal peak. (c) e^{-1} width calculated from equation (16) (red line) and from the model (black line). (d) Latitude of maximum westward wind speeds (red line) and latitude of maximum model DE3 amplitudes (black line). Note the general agreement between the red and black lines. Also note that the altitude where $\nu_r = \Omega$ (i.e., frequency of a diurnal tide in the absence of zonal mean winds) is $\sim$120 km, the same as the one found in the model (see Figure 6f).

Equation (12) has a solutions of the form

$$\hat{u} = F \exp\left(\frac{s\beta}{2a(\sigma_D - i\nu_r)}y^2\right). \tag{13}$$

If we then manipulate the exponential as

$$e^{\frac{c}{a-ib}} = e^{\frac{c}{a-ib}\frac{a+ib}{a+ib}} = e^{\frac{c(a+ib)}{a^2+b^2}} = e^{\frac{ca}{a^2+b^2}}e^{\frac{icb}{a^2+b^2}}, \tag{14}$$

where $a = \sigma_D$, $b = \nu_r$, and $c = \frac{s\beta}{2a}$, and consider the Doppler-shifted frequency $\sigma_D = \sigma + \frac{s\bar{U}}{a}$, we can write

$$\hat{u} = F \exp\left(\frac{s\beta\left(\sigma + \frac{s\bar{U}}{a}\right)}{2a\left[\left(\sigma + \frac{s\bar{U}}{a}\right)^2 + \nu_r^2\right]}y^2\right)\exp\left(i\frac{s\beta\nu_r}{2a\left[\left(\sigma + \frac{s\bar{U}}{a}\right)^2 + \nu_r^2\right]}y^2\right), \tag{15}$$

which, given that s is a negative value for the waves of interest (i.e., eastward propagating waves), is a Gaussian distribution with e^{-1} width equal to

$$e^{-1}_{\text{width}} = \left|\frac{2a\left[\left(\sigma + \frac{s\bar{U}}{a}\right)^2 + \nu_r^2\right]}{s\beta\left(\sigma + \frac{s\bar{U}}{a}\right)}\right|^{0.5}. \tag{16}$$

The relationship expressed in equation (15) for $\hat{u}$ describes the latitudinal shape of an equatorial wave with zero meridional wind, which is a function of ν_r and $\bar{U}$, both assumed to be a function of height. This dependency means that the width of the Gaussian distribution described by equation(16) also varies with height.

In the following subsection we use equations (15) and (16), the zonal mean winds as output from the model, and a vertical profile of a latitudinally independent Rayleigh friction coefficient to highlight some characteristics of upward propagating waves in the thermosphere. As explained below, the focus in this work is on the broadening of the latitude structures with height and on latitudinal asymmetries.

An implication of equation (15) is that for $\sigma_D \gg \nu_r$, the denominator goes to 0 when σ_D goes to 0. This is related to the difference between the phase speed $C_{ph} = \mathrm{d}\lambda/\mathrm{d}t$ (equal to $-n\Omega/s$ for a tide and $-\Delta\omega/m$ for a PW) and the mean wind U. As explained by *Salby et al.* [1984], waves generally need to have this quantity positive in order to propagate; the line where $C_{ph} = U$ is a critical line that wave does not easily cross. For DE3 and 3 day UFKW, $C_{ph} \approx 155$ m/s, while for SW$^-$, $C_{ph} = 349$ m/s, and SW$^+$, $C_{ph} = 87$ m/s. In the thermosphere this condition is not usually met, since zonal mean eastward wind speeds (i.e., superotation speeds) do not generally exceed 50 m/s [*Gasperini et al.*, 2016]. An additional implication of equation (15) is that a wave entering a region where $\nu_r > \sigma_D$ (i.e., heights greater than $\sim$110–130 km), transitions from an exponential growth (for propagating waves) or decay (for trapped oscillations) to an asymptotically constant value in the thermosphere (see the next section for more details on this).

3. Results: Mean Wind and Dissipation Effects

Figure 6 shows the height versus latitude structures of DE3 (i.e., a), 3 day UFKW (b), SW$^+$ (c), SW$^-$ (d) amplitudes in comparison to the zonal mean winds (e) for June solstice (i.e., DOY 171). We selected this day because the zonal mean winds are highly antisymmetric with respect to the equator, with westward maxima of 51 m/s around 30°S, and all the waves of interest are present and display large amplitudes, up to 26 K for DE3, 18 K for UFKW, 6 K for SW$^+$, and 6 K for SW$^-$. Figure 6f shows the vertical evolution of DE3 (red line), UFKW (blue line), SW$^+$ (green line), and SW$^-$ (yellow line) amplitudes at the latitude where the wind is maximum westward. Note that the winds are assumed positive to the east (i.e., blue colors in Figure 6e).

The vertical progression of DE3, UFKW, SW$^+$, and SW$^-$ amplitudes between 100 km and 260 km is presented in Figure 6f and shows that all the waves grow exponentially up to $\sim$120 km, the altitude where dissipation stops this growth and causes the amplitudes to decrease before reaching asymptotic values in the middle thermosphere. Above about 100 km, molecular diffusion is the dominant dissipation mechanism for vertically propagating waves. To gain some understanding of the vertical structure of upward propagating waves subject to molecular dissipation, *Lindzen* [1967b] defined the quantity $\chi = \left| \frac{4\pi^2}{\lambda_z^2} \frac{\nu_r}{\sigma} \right|$, where λ_z is vertical wavelength, to represent the ratio between diffusive and inertial forces. If we consider the frequency σ to be the Doppler-shifted frequency σ_D, we can express χ as

$$\chi = \left| \frac{4\pi^2}{\lambda_z^2} \frac{\nu_r}{\sigma_D} \right|. \tag{17}$$

When $\chi \sim 1$, dissipation is considered important to the local physics of the wave; thus, a wave entering this region transitions from an exponential growth (for propagating waves) or decay (for trapped oscillations) to asymptotically constant values in the thermosphere. The dependence of χ on λ_z^2 and σ_D is such that the altitude at which the molecular processes dominate increases with vertical wavelength (as λ_z^2) and wave frequency (as σ_D). For diurnal and semidiurnal tides, the altitude range at which $\chi \sim 1$ is approximately 100–170 km for vertical wavelengths in the range 30–150 km and similar altitudes for the UFKW with λ_z $\sim$50–70 km. As one can see from Figure 6f, DE3 and UFKW peak around 120 km, SW$^+$ peaks around 125 km, while SW$^-$ peaks around 115 km. The difference in peak altitude agrees with the vertical wavelength and frequency dependency of χ. For instance, SW$^+$ peaking higher than SW$^-$ can be explained by its higher frequency (1.33 day^{-1} versus 0.66 day^{-1}) and slightly longer vertical wavelength (41 km versus 38 km). Also, the zonal wave number plays a role, given that $\sigma_D = \sigma + (sU)/(a\cos\theta)$. SW$^+$ has $s = -4$, compared to $s = -2$ for SW$^-$, which indicates that the peak height of SW$^+$ is more sensitive to the background wind field.

In general, the effect of mean winds can be viewed as a distortion of the response compared to a windless case. For scalar variables (i.e., temperature) this means that the combination of Hough modes required to reconstruct the response is different than the combination of Hough modes comprising the forcing. The phrase "mode coupling" is utilized to describe the generation of modes (determined with orthogonal expansion of the calculated response) that are not forced directly by thermal excitation, but that arise due to the inseparability of the governing equations [*Lindzen and Hong*, 1974; *Walterscheid and Venkateswaran*, 1979a, 1979b; *Walterscheid et al.*, 1980; *Forbes and Garrett*, 1979]. It is often useful to consider the effect of mean winds on

an upward propagating wave simply by examining the implications of its Doppler-shifted frequency [*Forbes and Vincent*, 1989; *Forbes*, 2000]. For eastward propagating waves, the frequency is Doppler-shifted to higher absolute values in regions of westward wind ($U < 0$) and to lower absolute values in regions of eastward wind ($U > 0$). In regions where dissipation is important, waves with larger σ_D are less effectively damped than those with smaller σ_D.

A simple analytic expression for the equivalent depth h_n was derived by *Holton and Lindzen* [1968] specifically for Kelvin waves on an equatorial β plane. These authors showed that for a wave subject to mean winds $h_n = \frac{a\sigma_D^2}{gs^2}$, where g is Earth's gravitational acceleration. Waves propagating in the same (opposite) direction of the mean wind, i.e., Doppler shifted to lower (higher) absolute frequencies, experience a reduction (increase) in h_n, and thus a reduction (increase) in vertical wavelength, which results in increased (reduced) damping. Note that the change in vertical wavelength produces a reduction or increase in damping in the same direction as that expected for a change in the Doppler-shifted frequency [see *Forbes and Vincent*, 1989; *Ekanayake et al.*, 1997]. For instance, from equation (17) one can see that lower (higher) frequencies and shorter (longer) vertical wavelengths result in higher (lower) χ, thus increased (decreased) damping.

As displayed in Figure 6, the amplitude maxima tend to occur in the latitude region where the zonal mean winds are maximum westward, and the waves follow the westward wind regime up to 260 km. Note that DE3, UFKW, SW$^-$, and SW$^+$ are all eastward propagating, thus westward zonal mean winds Doppler-shift them to higher frequencies effectively reducing their susceptibility to dissipation. The behavior depicted in Figure 6 is consistent with the concept previously discussed that eastward (westward) propagating waves tend to be ducted toward westward (eastward) mean winds, and that Doppler shifting to higher (lower) frequencies reduces (increases) the effects of dissipation. The white dashed lines in Figures 6a–6d represent the e^{-1} width of the Gaussian distribution calculated using equation (15). The Rayleigh friction coefficient v_r was estimated using a vertical profile of ion drag for solar minimum conditions derived from *Richmond* [1970] and one from *Hickey et al.* [2011] of kinematic viscosity assuming an exospheric temperature of 877 K. (Note that the eddy diffusion was ignored, as a first-order approximation for the thermosphere). The e^{-1} width of each wave was calculated considering its vertical wavelength and, at each height, the Gaussian is centered at the latitude where the winds are maximum westward (this is the region of longest vertical wavelength and highest frequency). Above around 150 km molecular diffusion starts dominating, and consequently the waves' latitude structures do not vary appreciably with altitude, as shown by the contour lines that become vertical above around 150–180 km. For this reason, the white dashed lines in Figure 6 are depicted with a more faint color above 150 km. Note that, similar to DE3 and UFKW, the SW were also found to have small meridional wind components (i.e., SW$^-$ and SW$^+$ are also Kelvin waves), and thus equation 15 can be applied to these wave components as well.

Figures 7 and 8 present the same results as Figure 6, but for December solstice and March equinox, respectively. Comparing December solstice (i.e., Figure 7) to June solstice (i.e., Figure 6), one case see that the background wind field reverses from a westward jet of ∼50 m/s located in the Southern Hemisphere around 30°S to a westward jet located in the Northern Hemisphere of 65 m/s around 35°N. Similar to the June solstice case, all the waves exhibit a maximum near the latitude where the winds reach their largest westward magnitudes (i.e., around 10–35°N in the 110–130 km region) and tend follow the westward wind regime all the way up to 260 km. The March equinox case is presented in Figure 8 and displays a latitudinally symmetric wind field, with three westward maxima, at the equator and at ±50° latitude. For this case, the height-latitude structures of DE3, UFKW, SW$^+$, and SW$^-$ are largely symmetric with respect to the equator, especially compared to their structures during the solstices shown in Figures 6 and 7. Figures 7 and 8 further demonstrate the importance of the background wind field on the vertical propagation of global-scale wave through the thermosphere.

The vertical profile between 100 km and 200 km of the ion drag (blue line), the molecular viscosity (green line), and Rayleigh friction (black line) coefficient for DE3 is shown in Figure 9a. As previously discussed, the ion drag and molecular viscosity coefficients are derived from *Richmond* [1970] and *Hickey et al.* [2011], respectively, and refer to solar minimum conditions. The vertical profile of the zonal mean winds for June solstice, calculated as a ±20° average from the latitude of the westward peak, is shown in Figure 9b. The region where $v_r \sim \sigma_D$ is the region where dissipation becomes important to the local physics of an upward propagating wave. Neglecting ion drag (i.e., good approximation around 100–120 km, well below the *F* region ionospheric peak), one can show that the condition $v_r \approx \sigma_D$ is equivalent to $\chi = \left| \frac{4\pi^2}{\lambda_z^2} \frac{v_r}{\sigma_D} \right| \sim 1$, presented in equation (17).

The dependence of χ on λ_z^2 and σ_D is such that the altitude at which the molecular processes dominate increases with vertical wavelength and wave frequency. The black dashed vertical line in Figure 9a shows where the frequency is equal to Earth's rotation rate Ω. For a diurnal tide in the absence of zonal mean winds $\sigma_D \approx \sigma = \Omega$, thus the condition $\nu_r \approx \sigma_D$ is equivalent to $\nu_r \approx \Omega$, which in Figure 9a is the intercept between the black dashed line and the black solid line. As shown in Figure 9a, this altitude occurs around 120 km, which is consistent with what is found in the model (see Figure 6f).

Using the vertical profiles of Rayleigh friction (i.e., Figure 9a) and zonal mean winds (i.e., Figure 9b), we calculated the e^{-1} width of the Gaussian distribution from equation (16) as function of height (red solid line marked as "$U + \nu_r$" in Figure 9c) and compared it with the one calculated from the model (black line in Figure 9c). Using equation (16), the e^{-1} width of DE3 is found to be ~38° around 100 km, increasing to around 65° at 160 km, and reaching 80° at 200 km. For heights less than ~160 km, the similarities between the e^{-1} width calculated using equation (16) and the one found in the model are striking. Above ~150 km the model width and the one predicted using equation (16) start to differ, where the latter continues increasing and the former reaches a nearly asymptotic value of 65°. This difference is due to molecular diffusion effects departing from those modeled by equation (16). Note that the width depends not only on Rayleigh friction but also on the background winds. *Forbes* [2000] showed numerically that an eastward Kelvin wave that is Doppler shifted to a higher frequency (i.e., westward mean winds) is broader in latitude than the case where the frequency is Doppler shifted to lower values (i.e., in eastward mean winds). In order to understand the relative contribution of dissipation and mean winds in determining broadening, Figure 9c shows the e^{-1} width calculated by including only zonal mean winds (red dashed line, marked as U) and the e^{-1} that accounts for only Rayleigh friction (red dash-dotted line, marked as ν_r). Comparing the red dash-dotted line ($\nu_r{'}$) with the red solid line ("$U+\nu_r$"), one can see that the effect of mean winds is mostly negligible, accounting for only up to 7% at the height of maximum westward wind speeds (i.e., 115 km). Figure 9c demonstrates that the broadening of the latitude structures with height is largely an effect induced by dissipation.

Figure 9d displays the latitude of maximum as function of height correspondent to the latitude of maximum westward wind (red line) and as observed in the model (black line). The two lines share many similarities, with the latitude of maximum shifting to the Southern Hemisphere in the 100–120 km altitude range, moving back toward the equator for heights of 120–170 km, and reaching a constant value above 170–190 km. Figure 9d and the results shown in Figures 6–8 demonstrate that the latitudinal asymmetries are largely due to asymmetries in the background mean wind. Note that although Figure 9 refers to DE3, similar conclusions can be drawn for UFKW and the SW.

4. Conclusions

In this work we took advantage of a high-resolution TIME-GCM simulation for 2009 with the lower boundary based on MERRA reanalysis data, to demonstrate the existence and importance of SW generated by nonlinear interactions between DE3 and UFKW and their nature in terms of classical atmospheric wave theory. We found both primary and secondary waves to be large sources of day-to-day and latitude-longitude variability in the lower to the middle thermosphere and to vertically propagate in this height regime.

We then took an analytic approach toward investigating the effects of mean winds and dissipation on equatorially trapped global-scale waves, in order to isolate and elucidate the fundamental mechanisms governing certain features found in recent satellite observations [e.g., *Gasperini et al.*, 2015]. We applied the β-plane approximation to the momentum equations to show analytically how the vertical propagation of equatorially trapped Kelvin waves with zero meridional velocity (e.g., DE3, UFKW, SW⁻, and SW⁺) in a rotating atmosphere is affected by mean winds and dissipation.

The main results of this study can be summarized as follows:

1. The effect of molecular dissipation on upward propagating global-scale waves is to broaden the latitudinal structures in accord with prior theoretical predictions [e.g., *Volland and Mayr*, 1977; *Volland*, 1974] and satellite observations [e.g., *Gasperini et al.*, 2015], while zonal mean winds are found to be a negligible source of latitudinal broadening.

2. The main effect of background zonal mean winds on vertically propagating waves is to distort the height-latitude structures. Eastward propagating waves (i.e., DE3, UFKW, SW⁻, and SW⁺) show amplitude maxima in regions where the zonal mean winds are largest westward, and the waves tend to follow the

westward wind regime from the lower thermosphere up to the middle thermosphere. This finding is also in accord with the theory [e.g., *Forbes and Vincent*, 1989, *Forbes*, 2000] that westward (eastward) zonal mean winds Doppler-shift eastward propagating waves to higher (lower) frequencies and longer (shorter) vertical wavelength and thus are less affected by dissipation.

3. The altitude where upward propagating waves maximize is related to the ratio between the timescale for dissipation and the wave's Doppler-shifted frequency.

As demonstrated in this study, the combined effect of dissipation and zonal mean winds explains several of the noted differences in the height-latitude variability of DE3, UFKW, and their SW.

References

Angelats i Coll, M., and J. M. Forbes (2002), Nonlinear interactions in the upper atmosphere: The $s = 1$ and $s = 3$ nonmigrating semidiurnal tides, *J. Geophys. Res.*, *107*(A8), 1157, doi:10.1029/2001JA900179.

Beard, A. G., N. J. Mitchell, P. J. S. Williams, and M. Kunitake (1999), Non-linear interactions between tides and planetary waves resulting in periodic tidal variability, *J. Atmos. Sol. Terr. Phys.*, *61*, 363–376.

Cevolani, G., and S. Kingsley (1992), Non-linear effects on tidal and planetary waves in the lower thermosphere: Preliminary results, *Adv. Space Res.*, *12*(10), 77–80.

Chang, L. C., S. E. Palo, and H.-L. Liu (2009), Short-term variation of the $s = 1$ nonmigrating semidiurnal tide during the 2002 stratospheric sudden warming, *J. Geophys. Res.*, *114*, D03109, doi:10.1029/2008JD010886.

Chang, L. C., S. E. Palo, and H.-L. Liu (2011), Short-term variability in the migrating diurnal tide caused by interactions with the quasi 2 day wave, *J. Geophys. Res.*, *116*, D12112, doi:10.1029/2010JD014996.

Chapman, S., and R. S. Lindzen (1970), *Atmospheric Tides*, D. Reidel, Dordrecht, Holland.

Elhawary, R., and J. M. Forbes (2016), Planetary wave variability of Sq currents, *J. Geophys. Res. Space Physics*, *121*, 11,316–11,332, doi:10.1002/2016JA023242.

Ekanayake, E. M. P., T. Aso, and S. Miyahara (1997), Background wind effect on propagation of nonmigrating diurnal tides in the middle atmosphere, *J. Atmos. Sol. Terr. Phys.*, *59*, 401–429.

Forbes, J. M. (2000), Wave coupling between the lower and upper atmosphere: Case study of an ultra-fast Kelvin wave, *J. Atmos. Sol. Terr. Phys.*, *62*, 1603–1621.

Forbes, J. M., and H. B. Garrett (1979), Theoretical studies of atmospheric tides, *Rev. Geophys.*, *17*(8), 1951–1981, doi:10.1029/RG017i008p01951.

Forbes, J. M., and M. E. Hagan (1988), Diurnal propagating tide in the presence of mean winds and dissipation—A numerical investigation, *Planet. Space Sci.*, *36*(6), 579–590.

Forbes, J. M., and R. A. Vincent (1989), Effects of mean winds and dissipation on the diurnal propagating tide: An analytic approach, *Planet. Space Sci.*, *37*, 197–209.

Forbes, J. M., and Y. Moudden (2012), Quasi-two-day wave-tide interactions as revealed in satellite observations, *J. Geophys. Res.*, *117*, D12110, doi:10.1029/2011JD017114.

Forbes, J. M., and X. Zhang (2017), The quasi-6-day wave and its interactions with solar tides, *J. Geophys. Res. Space Physics*, 4764–4776, doi:10.1002/2017JA023954.

Forbes, J. M., S. L. Bruinsma, X. Zhang, and J. Oberheide (2009), Surface-exosphere coupling due to thermal tides, *Geophys. Res. Lett.*, *36*, L15812, doi:10.1029/2009GL038748.

Gasperini, F., and J. M. Forbes (2014), Lunar-solar interactions in the equatorial electrojet, *Geophys. Res. Lett.*, *41*, 3026–3031, doi:10.1002/2014GL059294.

Gasperini, F., J. M. Forbes, E. N. Doornbos, and S. L. Bruinsma (2015), Wave coupling between the lower and middle thermosphere as viewed from TIMED and GOCE, *J. Geophys. Res. Space Physics*, *120*, 5788–5804, doi:10.1002/2015JA021300.

Gasperini, F., J. M. Forbes, E. N. Doornbos, and S. L. Bruinsma (2016), Synthetic thermosphere winds based on CHAMP neutral and plasma density measurements, *J. Geophys. Res. Space Physics*, *121*, 3699–3721, doi:10.1002/2016JA022392.

Gu, S.-Y., X. Dou, J. Lei, T. Li, X. Luan, W. Wan, and J. M. Russell III (2014), Ionospheric response to the ultrafast Kelvin wave in the MLT region, *J. Geophys. Res. Space Physics*, *119*, 1369–1380, doi:10.1002/2013JA019086.

Hagan, M. E., A. Maute, and R. G. Roble (2009), Tropospheric tidal effects on the middle and upper atmosphere, *J. Geophys. Res.*, *114*, A01302, doi:10.1029/2008JA013637.

Harris, T. J., and R. A. Vincent (1993), The quasi-2-day wave observed in the equatorial middle atmosphere, *J. Geophys. Res.*, *98*, 10481–10490.

Häusler, K., M. E. Hagan, A. J. G. Baumgaertner, A. Maute, G. Lu, E. Doornbos, S. Bruinsma, J. M. Forbes, and F. Gasperini (2014), Improved short-term variability in the Thermosphere-Ionosphere-Mesosphere-Electrodynamics general circulation model, *J. Geophys. Res. Space Physics*, *119*, 6623–6630, doi:10.1002/2014JA020006.

Hickey, M. P., R. L. Walterscheid, and G. Schubert (2011), Gravity wave heating and cooling of the thermosphere: Sensible heat flux and viscous flux of kinetic energy, *J. Geophys. Res.*, *116*, A12326, doi:10.1029/2011JA016792.

Holton, J. R., and R. S. Lindzen (1968), A note on 'Kelvin' waves in the atmosphere, *Mon. Weather Rev.*, *96*, 385–386.

Kamalabadi, F., J. M. Forbes, N. A. Makarov, and Y. I. Portnyagin (1997), Evidence for non-linear coupling of planetary waves and tides in the Antarctic mesopause, *J. Geophys. Res.*, *102*, 4437–4446.

Lieberman, R. S., J. Oberheide, M. E. Hagan, E. E. Remsberg, and L. L. Gordley (2004), Variability of diurnal tides and planetary waves during November 1978–May 1979, *J. Atmos. Sol. Terres. Phys.*, *66*, 517–528.

Lindsay, R., M. Wensnahan, A. Schweiger, and J. Zhang (2014), Evaluation of seven different atmospheric reanalysis products in the arctic, *J. Clim.*, *27*, 2588–2606, doi:10.1175/JCLI-D-13-00014.1.

Lindzen, R. S. (1967a), Planetary waves on beta-planes, *Mon. Weather Rev.*, *95*(7), 441–451.

Lindzen, R. S. (1967b), Thermally driven diurnal tide in the atmosphere, *Q. J. R. Meteorol. Soc.*, *93*, 18–42.

Lindzen, R. S., and S. S. Hong (1974), Effects of mean winds and horizontal temperature gradients on solar and lunar semidiurnal tides in the atmosphere, *J. Atmos. Sci.*, *31*, 1421–1446.

Liu, H.-L., T. Li, C.-Y. She, J. Oberheide, Q. Wu, M. E. Hagan, J. Xu, R. G. Roble, M. G. Mlynczak, and J. M. Russell III (2007), Comparative study of short-term diurnal tidal variability, *J. Geophys. Res.*, *112*, D18108, doi:10.1029/2007JD008542.

Liu, H.-L., W. Wang, A. D. Richmond, and R. G. Roble (2010), Ionospheric variability due to planetary waves and tides for solar minimum conditions, *J. Geophys. Res.*, *115*, A00G01, doi:10.1029/2009JA015188.

Liu, H.-L., V. A. Yudin, and R. G. Roble (2013), Day-to-day ionospheric variability due to lower atmosphere perturbations, *Geophys. Res. Lett.*, *40*, 665–670, doi:10.1002/grl.50125.

Manson, A. H., C. E. Meek, J. B. Gregory, and D. K. Chakrabarty (1982), Fluctuations in tidal (24–12 h) characteristics and oscillations (5-25d) in the mesosphere and lower thermosphere at Saskatoon (52N, 107W), 1979-1981, *Planet. Space Sci.*, *30*, 1283.

Moudden, Y., and J. M. Forbes (2010), A new interpretation of Mars aerobraking variability: Planetary wave-tide interactions, *J. Geophys. Res.*, *115*, E09005, doi:10.1029/2009JE003542.

Moudden, Y., and J. M. Forbes (2011a), Simulated planetary wave-tide interactions in the atmosphere of Mars, *J. Geophys. Res.*, *116*, E01004, doi:10.1029/2010JE003698.

Moudden, Y., and J. M. Forbes (2011b), First detection of wave interactions in the middle atmosphere of Mars, *Geophys. Res. Lett.*, *38*, L04202, doi:10.1029/2010GL045592.

Moudden, Y., and J. M. Forbes (2013), A decade-long climatology of terdiurnal tides using TIMED/SABER observations, *J. Geophys. Res. Space Physics*, *118*, 4534–4550, doi:10.1002/jgra.50273.

Nguyen, V. A., S. E. Palo, R. S. Liebermann, J. M. Forbes, D. A. Ortland, and D. E. Siskind (2016), Generation of secondary waves arising from nonlinear interaction between the quasi 2 day wave and the migrating diurnal tide, *J. Geophys. Res. Atmos.*, *121*, 7762–7780, doi:10.1002/2016JD024794.

Oberheide, J., M. E. Hagan, R. G. Roble, and D. Offermann (2002), Sources of nonmigrating tides in the tropical middle atmosphere, *J. Geophys. Res.*, *107*(D21), 4567, doi:10.1029/2002JD002220.

Oberheide, J., J. M. Forbes, K. Häusler, Q. Wu, and S. L. Bruinsma (2009), Tropospheric tides from 80 to 400 km: Propagation, interannual variability, and solar cycle effects, *J. Geophys. Res.*, *114*, D00I05, doi:10.1029/2009JD012388.

Palo, S. E., R. G. Roble, and M. E. Hagan (1999), Simulation of the quasi-two-day wave using the TIME-GCM: Dynamical effects in the middle atmosphere, *Earth Planets Space*, *51*, 629–647.

Pancheva, D. V., and N. J. Mitchell (2004), Planetary waves and variability of the semidiurnal tide in the mesosphere and lower thermosphere over Esrange (68N, 21E) during winter, *J. Geophys. Res.*, *109*, A08307, doi:10.1029/2004JA010433.

Pancheva, D., A. G. Beard, N. J. Mitchell, and H. G. Muller (2000), Nonlinear interactions between planetary waves in the mesosphere lower thermosphere region, *J. Geophys. Res.*, *105*, 157–170.

Pancheva, D., et al. (2002), Global-scale tidal variability during the PSMOS campaign on June–August 1999: Interaction with planetary waves, *J. Atmos. Sol. Terr. Phys.*, *64*, 1865–1896.

Pedatella, N. M., and J. M. Forbes (2009), Modulation of the equatorial *F*-region by the quasi-16-day planetary wave, *Geophys. Res. Lett.*, *36*, L09105, doi:10.1029/2009GL037809.

Pedatella, N. M., and J. M. Forbes (2010), Evidence for stratosphere sudden warming-ionosphere coupling due to vertically propagating tides, *Geophys. Res. Lett.*, *37*, L11104, doi:10.1029/2010GL043560.

Pedatella, N. M., and J. M. Forbes (2012), The quasi 2 day wave and spatial-temporal variability of the OH emission and ionosphere, *J. Geophys. Res.*, *117*, A01320, doi:10.1029/2011JA017186.

Pedatella, N. M., H.-L. Liu, and M. E. Hagan (2012), Day-to-day migrating and nonmigrating tidal variability due to the six-day planetary wave, *J. Geophys. Res.*, *117*, A06301, doi:10.1029/2012JA017581.

Pogoreltsev, A. I., A. A. Vlasov, K. Frohlich, and C. Jacobi (2007), Planetary waves in coupling the lower and upper atmosphere, *J. Atmos. Sol. Terr. Phys.*, *69*, 2083–2101.

Richmond, A. D., E. C. Ridley, and R. G. Roble (1992), A thermosphere/ionosphere general circulation model with coupled electrodynamics, *Geophys. Res. Lett.*, *19*, 601–604.

Richmond, A. D. (1970), Geomagnetic crochets and ionospheric tidal winds, PhD thesis, Univ. Calif., Los Angeles, Calif.

Rienecker, M. M., et al. (2011), MERRA: NASA's Modern-Era Retrospective Analysis for Research and Applications, *J. Clim.*, *24*, 3624–3648, doi:10.1175/JCLI-D-11-00015.1.

Roble, R. G., and E. C. Ridley (1994), A thermosphere-ionosphere-mesosphere-electrodynamics general circulation model (TIME-GCM): Equinox solar cycle minimum simulations (30–500 km), *Geophys. Res. Lett.*, *21*, 417–420.

Roble, R. G., E. C. Ridley, A. D. Richmond, and R. E. Dickinson (1988), A coupled thermosphere/ionosphere general circulation model, *Geophys. Res. Lett.*, *15*, 1325–1328.

Salby, M. L., D. L. Hartmann, P. L. Bailey, and J. C. Gille (1984), Evidence for equatorial Kelvin modes in Nimbus-7 LIMS, *J. Atmos. Sci.*, *41*, 220–235, doi:10.1175/1520-0469(1984)041<0220:EFEKMI>2.0.CO;2.

Teitelbaum, H., and F. Vial (1991), On tidal variability induced by nonlinear interaction with planetary waves, *J. Geophys. Res.*, *96*, 14,169–14,178.

Thayaparan, T., W. K. Hocking, and J. MacDougal (1997a), Amplitude, phase and period variations of the quasi 2-day wave in the mesosphere and lower thermosphere over London Ontario (43N, 81W), during 1993 and 1994, *J. Geophys. Res.*, *102*, 9461–9478.

Thayaparan, T., W. K. Hocking, J. MacDougal, A. H. Manson, and C. E. Meek (1997b), Simultaneous observations of the 2-day wave at London Ontario (43N, 81W) and Saskatoon (52N, 107W) near 91 km altitude during the two years 1993 and 1994, *Ann. Geophys.*, *15*, 1324–1339.

Truskowski, A. O., J. M. Forbes, X. Zhang, and S. E. Palo (2014), New perspectives on thermosphere tides—1. Lower thermosphere spectra and seasonal-latitudinal structures, *Earth Planets Space*, *66*(136), doi:10.1186/s40623-014-0136-4.

Vial, F., and H. Teitelbaum (1984), Some consequences of turbulent dissipation on the diurnal thermal tide, *Planet. Space Sci.*, *32*, 1559.

Volland, H. (1974), Solutions of Laplace's tidal equation for complex frequencies, *J. Atmos. Sol. Terr. Phys.*, *36*, 445–460, doi:10.1029/RG015i002p00203.

Volland, H., and H. G. Mayr (1977), Theoretical aspects of tidal and planetary wave propagation at thermospheric heights, *Rev. Geophys.*, *15*(2), 203–226, doi:10.1029/RG015i002p00203.

Walterscheid, R. L., and S. V. Venkateswaran (1979a), Influence of mean zonal motion and meridional temperature gradients on the solar semidiurnal atmospheric tide: A spectral study. Part I: Theory, *J. Atmos. Sci.*, *36*, 1623–1635.

Walterscheid, R. L., and S. V. Venkateswaran (1979b), Influence of mean zonal motion and meridional temperature gradients on the solar semidiurnal atmospheric tide: A spectral study. Part I: Numerical results, *J. Atmos. Sci.*, *36*, 1636–1662.

Walterscheid, R. L., J. G. de Vore, and S. V. Venkateswaran (1980), Influence of mean zonal motion and meridional temperature gradients on the solar semidiurnal tide: A revised spectral study with improved heating rates, *J. Atmos. Sci.*, *37*, 455–470.

Yamashita, K., S. Miyahara, Y. Miyoshi, K. Kawano, and J. Ninomiya (2002), Seasonal variation of non-migrating semidiurnal tide in the polar MLT region in a general circulation model, *J. Atmos. Sol. Terr. Phys.*, *64*, 1083–1094.

Yue, J., W. Wang, A. D. Ricshmond, H.-L. Liu, and L. C. Chang (2013), Wavenumber broadening of the quasi 2 day planetary wave in the ionosphere, *J. Geophys. Res. Space Physics*, *118*, 3515–3526, doi:10.1002/jgra.50307.